

# LLM4SG: Large Language Models for Scatterer Generation via Synesthesia of Machines

Zengrui Han, *Graduate Student Member, IEEE*, Lu Bai, *Member, IEEE*, Ziwei Huang, *Member, IEEE*, and Xiang Cheng, *Fellow, IEEE*

**Abstract**—Guided by Synesthesia of Machines (SoM), the non-linear mapping relationship between sensory and communication information serves as a powerful tool to enhance both the accuracy and generalization of vehicle-to-vehicle (V2V) multi-modal intelligent channel modeling (MMICM) in intelligent transportation systems (ITSs). To explore the general mapping relationship between physical environment and electromagnetic space, a new intelligent sensing-communication integration dataset, named V2V-M3, is constructed for multiple scenarios in V2V communications with multiple frequency bands and multiple vehicular traffic densities (VTDs). Leveraging the strong representation and cross-modal inference capabilities of large language models (LLMs), a novel LLM-based method for Scatterer Generation (LLM4SG) from light detection and ranging (LiDAR) point clouds is developed. To address the inherent and significant differences across multi-modal data, synergistically optimized four-module architecture, i.e., preprocessor, embedding, backbone, and output modules, are designed by considering the sensing/channel characteristics and electromagnetic propagation mechanism. On the basis of cross-modal representation alignment and positional encoding, the network of LLM4SG is fine-tuned to capture the general mapping relationship between LiDAR point clouds and scatterers. Simulation results demonstrate that the proposed LLM4SG achieves superior performance in full-sample and generalization testing, significantly outperforming small models across different frequency bands, scenarios, and VTDs.

**Index Terms**—Large language model (LLM), Synesthesia of Machines (SoM), multi-modal intelligent channel modeling (MMICM), V2V-M3 dataset, fine-tuning.

## I. INTRODUCTION

VEHICLE-TO-VEHICLE (V2V) communication network is an essential component of intelligent transportation systems (ITSs), which can support various advanced applications for intelligent vehicles [1], [2]. To ensure the safety and efficiency of connected and autonomous vehicles in ITSs, the development of sixth-generation (6G) V2V communications requires an in-depth understanding of the environment and accurate V2V channel modeling [3]. Current V2V channel models generally fall into two categories, i.e., stochastic models and deterministic models. Stochastic models utilize statistical approaches to randomly generate and determine channel parameters [4], [5]. Nonetheless, stochastic models

are computationally efficient, and the reliance on randomness limits their accuracy. In contrast, deterministic models mimic the physical radio propagation process in specific environments, which offer high precision while at the cost of significant computational complexity [6], [7]. As a result, neither approach strikes an ideal trade-off between accuracy and complexity, which poses challenges for the design of 6G V2V communication networks in ITSs.

As artificial intelligence (AI) technology continues to develop rapidly, researchers have proposed many AI-based channel models [8]. Unlike conventional methods, AI technology significantly facilitates the trade-off between modeling accuracy and complexity, benefiting from the superior ability to extract patterns from massive data. To overcome the challenges associated with dynamic V2V communications, a method for multipath component (MPC) clustering was proposed in [9]. Due to the rapidly changing environment, the MPC tracking was conducted through Kalman filtering and Kuhn-Munkres algorithm, which recognized dynamic behaviors of MPCs and time-varying clusters. To further achieve real-time angle-of-angle (AoA) prediction in high-mobility V2V communications, the authors in [10] proposed a fast multilayer perceptron (MLP)-based AoA recognition model, which includes offline training and online estimation phases. Despite the progress made in [9] and [10], further exploration is required in V2V channel modeling utilizing artificial neural networks (ANNs), which provide powerful capabilities. The authors in [11] adopted an ANN-driven V2V channel model to recognize the path loss and shadowing. To further ensure robustness under varying channel conditions, a generative adversarial network (GAN) and feedforward neural network (FNN) based V2V channel model was proposed in [12] and was utilized to predict the probability density function (PDF) and power of received signals. Furthermore, a V2V channel measurement campaign was carried out and a GAN-based channel model was proposed in [13] based on the channel measurement data. Consequently, the proposed channel models in [9]–[13] demonstrated that the employment of AI technologies could improve the accuracy of the V2V channel models in ITSs. However, the aforementioned studies relied exclusively on uni-modal radio-frequency (RF) communication data, which provides a limited understanding of the surrounding propagation environment leading to the limited accuracy of V2V channel modeling. Meanwhile, the aforementioned models depend on specific scenario data without a comprehensive understanding of the environment, limiting the ability to generalize across diverse scenarios and conditions.

Z. Han, Z. Huang, and X. Cheng are with the State Key Laboratory of Photonics and Communications, School of Electronics, Peking University, Beijing, 100871, P. R. China (email: zengruihan@stu.pku.edu.cn, ziwei-huang@pku.edu.cn, xiangcheng@pku.edu.cn).

L. Bai is with the Joint SDU-NTU Centre for Artificial Intelligence Research (C-FAIR), Shandong University, Jinan, 250101, P. R. China (e-mail: lubai@sdu.edu.cn).

Currently, integrated sensing and communications (ISAC) [14]–[16] has received wide attention in 6G V2V communications. ISAC has demonstrated the potential mutual enhancement between sensing and communications based on the potential mapping relationship between the physical environment and the electromagnetic space. Fortunately, not limited to RF sensing and communications, connected and autonomous vehicles in ITSs will be simultaneously equipped with multi-modal non-RF and RF devices, e.g., non-RF light detection and ranging (LiDAR) and RF communication equipment. Compared to RF sensing, LiDAR offers higher resolution, more accurate three-dimensional (3D) modeling, and superior detection of static objects, thus making it a powerful tool for detailed environmental sensing. To comprehensively utilize the multi-modal information from communication devices and sensors, inspired by synesthesia of human, a novel concept, i.e., Synesthesia of Machines (SoM), was proposed by Cheng et al. [17]. Motivated by SoM, multi-modal intelligent channel modeling (MMICM) has been regarded as a new modeling paradigm [18]. The nonlinear mapping relationship between sensory and communication information, which tightly integrates environmental features into channel modeling, constitutes an essential part of MMICM. For instance, leveraging sensory information to predict electromagnetic scatterers enables more precise characterization of the propagation environment, thereby substantially enhancing channel modeling accuracy. In [19], we preliminarily explored the mapping relationship between LiDAR point clouds and scatterers and proposed a novel 6G V2V channel model with improved accuracy. However, our previous work was designed on a specific scenario based on small models with few parameters, which constrains its generalization potential to meet the demands of diverse V2V applications [19]. As a result, there is an urgent need for V2V channel models with better generalization capabilities for diverse scenarios and varying conditions.

Large language models (LLMs), which have revolutionized the field of natural language processing (NLP), have been successfully applied across domains [20] and are capable of performing few-shot [21] or zero-shot learning. Especially, LLMs exhibit significant adaptability on cross-modal downstream tasks of channel prediction [22], [23] through fine-tuning, where smaller training datasets are adopted and fewer parameters are adjusted. Owing to the Transformer-based architecture with self-attention mechanisms, LLMs are capable of integrating multi-modal inputs and modeling complex nonlinear relationships, which closely aligns with aforementioned mapping relationship exploration. Recognizing the strong generalization and reasoning abilities of LLMs, we attempt to utilize LLMs to improve the generalization capabilities of V2V channel models. To be specific, based on a new intelligent sensing-communication dataset, a novel LLM-based method for Scatterer Generation (LLM4SG) from LiDAR point clouds is developed. A four-module architecture is carefully designed to tailor the LLM to the scatterer generation task. Leveraging the powerful capabilities of LLMs, the explored mapping relationship between LiDAR point clouds and scatterers exhibits robust generalizability across multiple ITS scenarios with multiple frequency bands and multiple vehicular traffic

densities (VTDs). It demonstrates the advantages of LLMs over small models in handling complex tasks and adapting to dynamic environments. The major contributions and novelties of this paper are summarized as follows.

- 1) Accurate scatterer generation from sensory data is pivotal for V2V MMICM, unlike conventional models that rely on statistical distributions to generate scatterers randomly. However, the inherent complexity and significant disparities in multi-modal data present substantial challenges. To address this, we propose LLM4SG to adapt pre-trained LLMs to explore a general mapping relationship between LiDAR point clouds and scatterers in ITSs for the first time.
- 2) We develop V2V-M3, a comprehensive V2V dataset for intelligent sensing-communication integration. V2V-M3 encompasses diverse ITS scenarios (e.g., urban, suburban) to meet varied application needs, incorporates multiple frequency bands (e.g., 28 GHz, sub-6 GHz) due to the significant and nonlinear variations in propagation characteristics across frequencies, and includes multiple VTDs (e.g., low, high) as a critical factor influencing V2V channel properties. Unlike datasets designed for small models that focus on the specific scenario condition, the V2V-M3 dataset is constructed to train and validate the accuracy and generalization capabilities of most of the related work across a wide range of scenario conditions.
- 3) LLM4SG employs a synergistically optimized four-module architecture, i.e., preprocessor, embedding, backbone, and output modules, to explore complex nonlinear mapping relationship between LiDAR point clouds and scatterers. The preprocessor standardizes LiDAR point clouds under varying conditions, while the embedding module aligns the feature space of LLMs through cross-modal representation alignment and positional encoding, preserving critical physical and electromagnetic information. Building on this foundation, the backbone network is fine-tuned and combined with the output module to accurately capture the general mapping relationship in multiple ITS scenarios with multiple frequency bands and multiple VTDs.
- 4) By virtue of precise alignment processing of multi-modal data and efficient adaptation to LLMs, LLM4SG delivers outstanding performance and generalization in scatterer generation. It achieves over 93% accuracy in position generation and over 85% in quantity generation. The innovative four-module architecture significantly enhances knowledge transfer across VTDs, frequency bands, and ITS scenarios, demonstrating superior generalization capabilities and outperforming smaller models by more than 9%.

The remainder of this paper is organized as follows. Section II introduces the intelligent sensing-communication integration dataset V2V-M3. The LLM4SG, which can explore the generalized mapping relationship between the physical environment and electromagnetic space, is developed in Section III. In Section IV, simulation settings are illustrated and then the

performance of the proposed LLM4SG method on full-sample and generalization testing is evaluated. Finally, Section V draws the conclusion.

## II. V2V-M3 DATASET CONSTRUCTION

In this section, a new high-fidelity intelligent sensing-communication integration simulation V2V dataset, named V2V-M3, for multiple ITS scenarios with multiple frequency bands and multiple VTDs is constructed. To achieve the synchronous collection of the sensing and communication data, two high-fidelity simulation software, i.e., Wireless InSite [24] and AirSim [25], are intelligently incorporated as an integrated platform [26] to achieve in-depth integration and precise alignment. Wireless InSite employs the ray-tracing (RT) technology to mimic radio wave propagation and collect channel data. AirSim is an open-source platform developed on Unreal Engine and is used to collect high-fidelity sensing data, such as LiDAR point clouds. The V2V-M3 dataset is designed to simulate diverse V2V communication conditions, which are challenging to capture in real-world measurements. It covers various scenarios, including urban and suburban, employs 5.9 GHz and 28 GHz frequency bands, and accounts for different traffic density levels, including low and high VTDs. The V2V-M3 dataset supports comprehensive testing and validation efforts, with the potential to contribute to broader research in V2V communications. Specific scenario configurations and data collection are given as follows.

### A. Scenario Configuration

Two typical V2V scenarios are constructed, i.e., an urban crossroad and a suburban forking road. The urban crossroad is surrounded by tall and densely packed buildings, which bring unique challenges, such as significant signal obstruction and multipath propagation. In contrast, buildings are fewer and more spread out in the suburban forking road, resulting in line-of-sight (LoS) communications and different propagation characteristics. Urban and suburban scenarios encompass rich and sparse scattering environments, which provide a comprehensive representation of typical V2V communications. This diversity not only captures the distinct challenges encountered in different environment, but also enhances the generalization capability of the proposed model. As a result, the following observation is applicable across a broad spectrum of real-world V2V communication scenarios.

Physical environments for the two scenarios are precisely rendered in AirSim. Then, 3D models in physical environments are properly imported from AirSim into Wireless InSite to achieve precise alignment. As a consequence, electromagnetic space, which aligns with the physical environment, is established in Wireless InSite. Fig. 1 and Fig. 2 presents urban crossroad and suburban forking road scenarios under different VTDs in AirSim and Wireless InSite. In Fig. 1(a) and Fig. 2(a), the high-fidelity physical environment of the crossroad and forking road in AirSim is illustrated. Fig. 1(b) and Fig. 2(b) depict the corresponding electromagnetic space in Wireless InSite, where a precise alignment with scenarios in AirSim is implemented. Note that investigation of the impact of VTDs

on V2V communications is vital for the resilient ITS design, which can support sixth-generation (6G) applications, such as target localization and autonomous vehicle tracking. High VTDs result in increased interactions among vehicles, which can affect signal quality and communication reliability. In this case, crossroad and forking road scenarios contain high and low VTDs. The numbers of vehicles on the crossroad under high and low VTDs are 20 and 12, respectively. The numbers of vehicles on the forking road under high and low VTDs are 15 and 8, respectively.

### B. Data Collection

The number of snapshots is set to 1500 for each VTD condition in each scenario. First, initial positions of all vehicles are generated in AirSim, and the setup in Wireless InSite is precisely aligned with them. Then, 3D coordinates of vehicles are set snapshot by snapshot in AirSim to mimic vehicular movement. In Wireless InSite, by analyzing internal files and batch revising 3D coordinates of vehicles, vehicular trajectories are aligned snapshot by snapshot with those in AirSim. For clarity, vehicular trajectories under high and low VTDs in the crossroad and forking road are shown in Fig. 1(c) and Fig. 2(c).

Each vehicle follows a distinct trajectory, speed, and movement duration to construct dynamic and complex V2V scenarios. Additionally, each vehicle is equipped with a LiDAR and a communication unit, where sensor and transceiver positions and vehicular trajectories are precisely aligned. The LiDAR in AirSim features 16 channels with a scanning frequency of 10 Hz. High-fidelity LiDAR point clouds are obtained for each vehicle at each snapshot in AirSim. The communication unit in Wireless InSite is operated with typical mmWave and sub-6 GHz frequency bands, i.e.,  $f_c = 28$  GHz carrier frequency with 2 GHz communication bandwidth and  $f_c = 5.9$  GHz carrier frequency with 20 MHz communication bandwidth. Each communication unit includes a transmitter (Tx) and a receiver (Rx), and the numbers of antennas at Tx and Rx are  $M_T = M_R = 1$ . By utilizing the RT technology, electromagnetic propagation scatterers and channel impulse response (CIR) data are generated for 18 pairs of V2V links under each VTD condition in the crossroad and forking road.

## III. LLM FOR MULTI-MODAL INTELLIGENT V2V CHANNEL MODELING

In this section, we propose LLM4SG, which is designed to explore the generalized mapping relationship between physical environment and electromagnetic space. The LLM4SG algorithm leverages the powerful reasoning capabilities of LLMs to recognize scatterers by extracting meaningful insights from LiDAR point clouds. To mitigate the feature space gap between sensing/channel data and language data, specific modules are designed in LLM4SG, which contain preprocessor, embedding, backbone, and output modules. The preprocessor module refines the raw input LiDAR point clouds, preparing it for subsequent stages. Next, the embedding module converts LiDAR point cloud features and frequency band feature into a format compatible with LLMs. The backbone then extracts

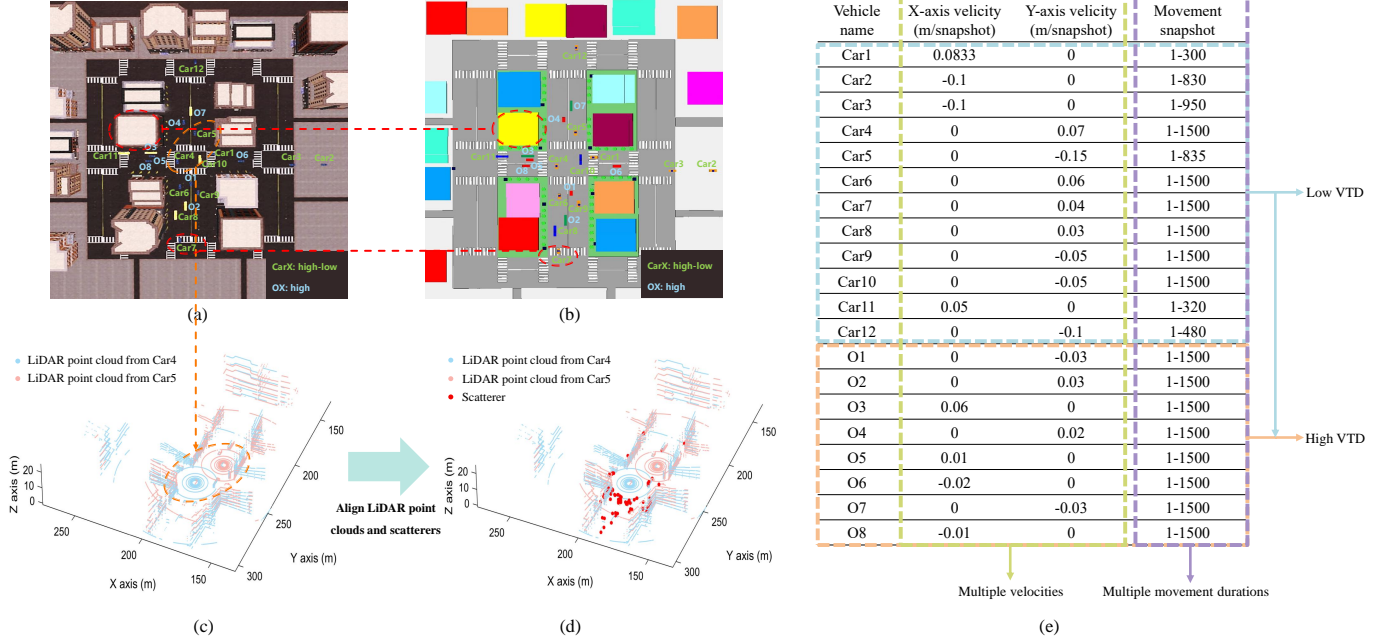


Fig. 1. Crossroads in AirSim and Wireless InSite and detailed parameter setting of vehicular trajectories under high and low VTDs. (a) Crossroad in AirSim under high and low VTDs at Snapshot 800. (b) Crossroad in Wireless InSite under high and low VTDs at Snapshot 800. (c) Combined LiDAR point clouds from Tx and Rx in AirSim. (d) Alignment between LiDAR point clouds and scatterers. (e) Detailed parameter setting of vehicular trajectories under high and low VTDs.

high-level features essential for accurate scatterer generation. Finally, the output module utilizes output features to generate precise scatterer grid maps. The network components, as shown in Fig. 3, and the training process are illustrated below.

#### A. Preprocessor Module

The extensive data in LiDAR point clouds leads to high computational complexity, and noise and redundant points interfere with feature extraction and mapping relationship exploration. Meanwhile, there are inherent and significant differences between LiDAR point clouds and scatterers in terms of collection frequency bands and application significance resulting in the huge challenge of mapping relationship exploration. To address the aforementioned challenges, a pre-processor module is applied to eliminate excess information and retain essential data. The module includes concatenation and filtering of LiDAR point clouds and feature extraction.

In this process, to share the observed physical environment, LiDAR point clouds obtained from transceivers are concatenated. Subsequently, ground points in LiDAR point clouds generated from the laser reflection off the ground are removed based on a threshold  $H_G$ . This step is essential as ground points typically contains a large portion of LiDAR point clouds and appear as a texture that significantly interferes with feature extraction. Then, LiDAR point clouds undergo visibility region (VR) [27] filtering, which is widely used in channel modeling. To be specific, scatterers are visible and contribute to channel characterization only if they are within the VR. In [27], the VR is defined as an ellipsoid with the Tx and Rx as its two focuses. The major axis  $2a(t)$  of the ellipsoid is calculated as the sum of the distances from

the scatterers to transceivers. The minor axis  $2b(t)$  and the focal length  $2c(t)$  are equal to the distance  $D_T(t)$  between transceivers. As a result, processed LiDAR point clouds retain effective environmental information associated with vehicles, buildings, and trees within VR. Processed LiDAR point clouds are expressed as

$$\mathbb{P}(t) = \{\mathbf{C}(t) | \mathbf{C}(t) = [x_L(t), y_L(t), z_L(t)]\}. \quad (1)$$

Feature extraction of processed LiDAR point clouds is further conducted. In fact, RT effectively identifies scatterers by simulating paths and interactions of rays in a 3D environment. Therefore, when extracting features from LiDAR point clouds, we consider factors similar to those in RT, such as object geometry, material properties, and interaction angles. As a consequence, the widely used grid feature extraction technique [28] in computer vision and image processing is leveraged. LiDAR point clouds  $\mathbb{P}(t)$  are divided into a grid map with a dimension of  $m^x \times m^y$ . The length and width of each grid can be calculated as

$$x_g(t) = \frac{x_{\max}(t) - x_{\min}(t)}{m^x} \quad (2)$$

$$y_g(t) = \frac{y_{\max}(t) - y_{\min}(t)}{m^y} \quad (3)$$

where  $x_{\min}(t)$ ,  $x_{\max}(t)$ ,  $y_{\min}(t)$ , and  $y_{\max}(t)$  are extreme values of LiDAR point clouds  $\mathbb{P}(t)$  in  $x$ -axis and  $y$ -axis directions. Each grid is determined by four coordinates, i.e.,  $(x_{\min}^g(t), y_{\min}^g(t))$ ,  $(x_{\min}^g(t), y_{\max}^g(t))$ ,  $(x_{\max}^g(t), y_{\min}^g(t))$ ,  $(x_{\max}^g(t), y_{\max}^g(t))$ . LiDAR point clouds within each grid are given as

$$\mathbb{P}^g(t) = \{\mathbf{C}(t) | x_{\min}^g(t) \leq x_L(t) < x_{\max}^g(t), y_{\min}^g(t) \leq y_L(t) < y_{\max}^g(t)\}. \quad (4)$$

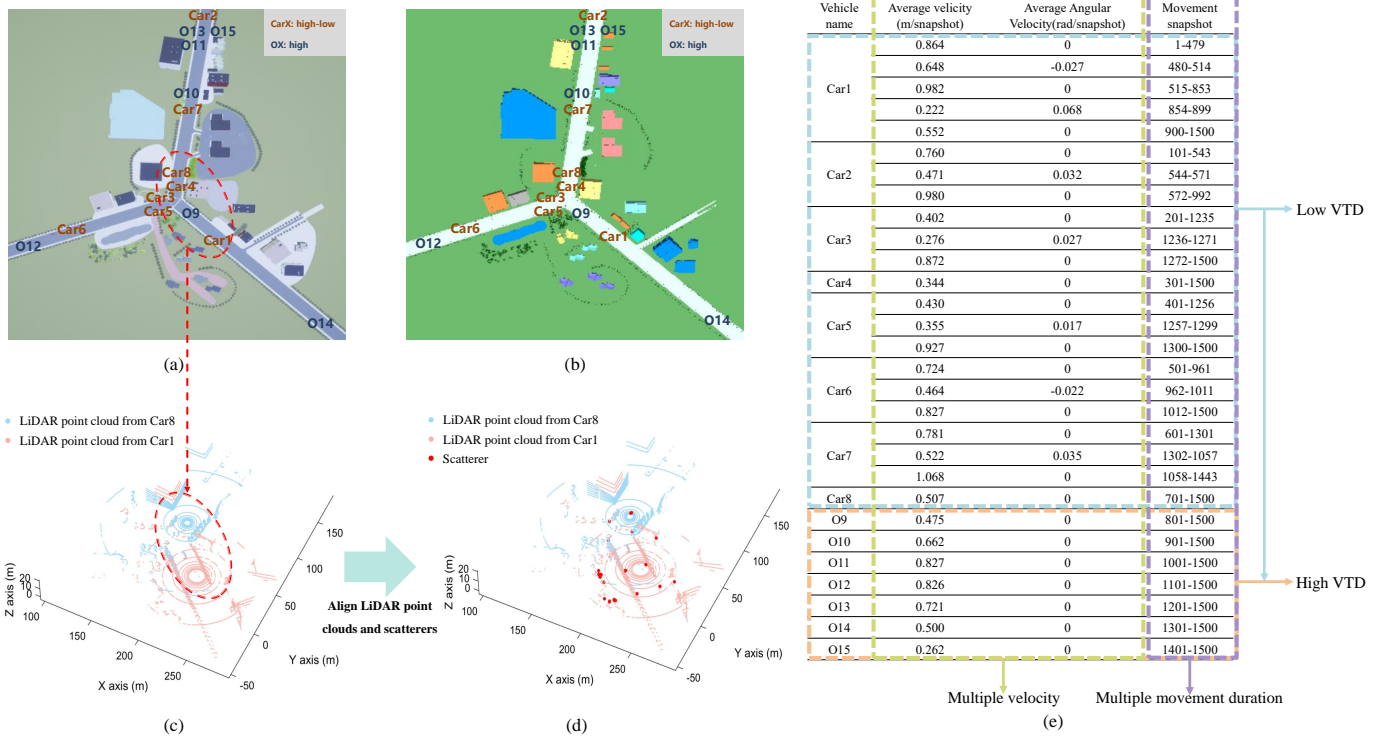


Fig. 2. Forking roads in AirSim and Wireless InSite and detailed parameter setting of vehicular trajectories under high and low VTDs. (a) Forking road in AirSim under high and low VTDs at Snapshot 1230. (b) Forking road in Wireless InSite under high and low VTDs at Snapshot 1230 (Vehicles which have not yet entered the scenario are labeled with initial positions). (c) Combined LiDAR point clouds from Tx and Rx in AirSim. (d) Alignment between LiDAR point clouds and scatterers. (e) Detailed parameter setting of vehicular trajectories under high and low VTDs.

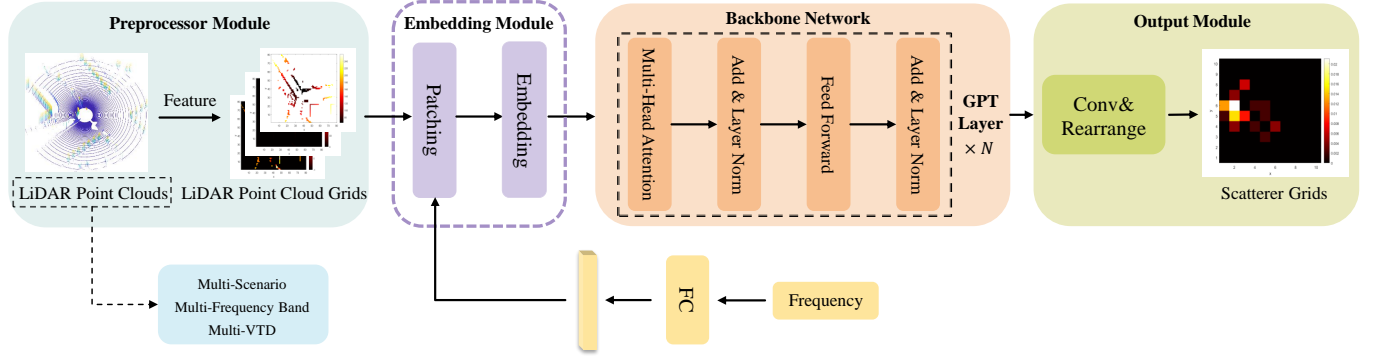


Fig. 3. An illustration of the network architecture of LLM4SG.

Then, feature grid map  $\mathbf{F} \in \mathbb{R}^{m^x \times m^y \times H}$  of LiDAR point clouds  $\mathbb{P}(t)$  is extracted, where  $H$  is the number of channels. The first channel  $\mathbf{F}^1$  of feature grid map  $\mathbf{F}$  is the density of LiDAR point clouds in each grid, which can be calculated as

$$\rho_g(t) = \frac{|\mathbb{P}^g(t)|}{x_g(t) \times y_g(t)} \quad (5)$$

where  $|\cdot|$  denotes the number of elements in a set. The channel  $\mathbf{F}^1$  represents a visual depiction of the scenario layout, which shows the distribution of scatterer-related elements, such as buildings, vehicles, and trees. Next, the second channel  $\mathbf{F}^2$  of feature grid map  $\mathbf{F}$  is the maximum height of LiDAR point clouds in each grid, which can be calculated as

$$h_g(t) = \max_{\mathbf{C}(t) \in \mathbb{P}^g(t)} z_L(t). \quad (6)$$

The channel  $\mathbf{F}^2$  provides 3D information related to the environment. Finally, the third channel  $\mathbf{F}^3$  of feature grid map  $\mathbf{F}$  is the distance from the transceiver to LiDAR point clouds in each grid, which can be calculated as

$$d_g(t) = \frac{d_g^T(t) + d_g^R(t)}{2} \quad (7)$$

where  $d_g^T(t)$  denotes the distance between the center of each grid and Tx and  $d_g^R(t)$  denotes the distance between the center of each grid and Rx. The channel  $\mathbf{F}^3$  is similar to a position encoding layer, which further enhances the understanding of distance effects on scatterer distribution.

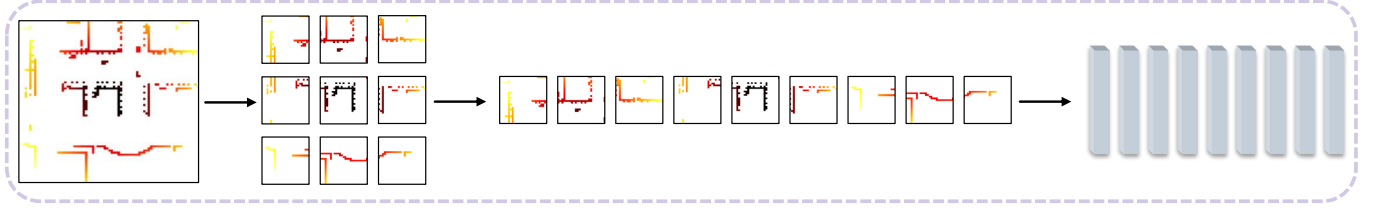


Fig. 4. An illustration of the patching operation of LiDAR point cloud features.

### B. Embedding Module

In general, the mainstream LLM is based on the Transformer architecture [29], which has demonstrated remarkable effectiveness in large-scale language tasks. The self-attention mechanism of Transformer enables the model to capture long-range dependencies in the text by attending to relevant tokens regardless of their position within the sequence. In this architecture, the embedding module plays a key role in transforming raw input data into a format optimized for the network. By converting the data into a fixed-dimensional latent space, the module ensures a consistent representation across all layers. To be specific, the embedding module includes patch embedding and positional embedding, specifically designed to better adapt communication data and sensing data to LLMs. The module further captures the global relationships between different regions of LiDAR point clouds while preserving positional information. This overcomes the receptive field limitations of conventional CNNs in image processing, enabling a more effective learning of electromagnetic propagation mechanisms.

The standard Transformer takes a one-dimensional (1D) sequence of token embeddings as input. For the two-dimensional (2D) LiDAR point cloud feature, we convert the feature grid map  $\mathbf{F} \in \mathbb{R}^{m^x \times m^y \times H}$  into a sequence of flattened 2D patches  $\mathbf{F}_p$ , as shown in Fig. 4, which can be expressed as

$$\mathbf{F}_p = \mathcal{V}(\mathcal{C}(\mathbf{F})) \in \mathbb{R}^{N \times (Q^2 \times H)} \quad (8)$$

where  $\mathcal{C}(\cdot)$  and  $\mathcal{V}(\cdot)$  represent a convolutional layer and a reshape operation, respectively.  $(Q, Q)$  is the resolution of each patch and  $N$  is the resulting number of patches, which can be calculated as

$$N = \frac{m^x \times m^y}{Q^2}. \quad (9)$$

As the Transformer maintains constant latent vector size  $D$  through all layers, patches are flattened and mapped to  $D$  dimensions with a trainable linear mapping, which can be expressed as

$$\mathbf{F}_d = \mathcal{L}(\mathbf{F}_p) \in \mathbb{R}^{N \times D} \quad (10)$$

where  $\mathcal{L}(\cdot)$  represents a linear layer.

Since the Transformer processes inputs in parallel rather than sequentially, it lacks an inherent sense of token positions within a sequence. By adding a position-based vector to each token, position embeddings allow the model to recognize relative/absolute positions of LiDAR point cloud tokens, which provide crucial context for understanding sequences. A learnable 1D positional encoding  $\mathbf{F}^{\text{PE}} \in \mathbb{R}^{N \times 1}$  is implemented to facilitate the capturing of spatial information, which is

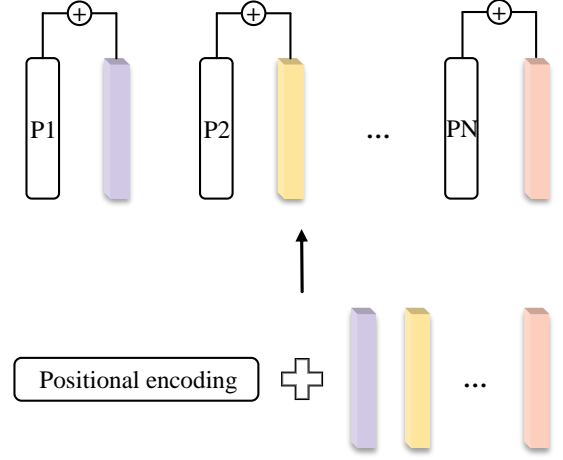


Fig. 5. An illustration of the position encoding.

shown in Fig. 5. To incorporate positional encoding into patch embeddings, the positional encoding is broadcasted to the same dimension as  $\mathbf{F}_d$  and can be given by  $\tilde{\mathbf{F}}^{\text{PE}} \in \mathbb{R}^{N \times D}$ . Then, positional encoding is added to the patch embeddings, which can be expressed as

$$\mathbf{F}_d^{\text{PE}} = \mathbf{F}_d + \tilde{\mathbf{F}}^{\text{PE}}. \quad (11)$$

Position embeddings enable the model not only to incorporate positional context but also to adaptively focus on the most relevant patches within the LiDAR point clouds.

Furthermore, due to huge differences in the collection frequency bands between sensing data and communication data, the communication frequency information is not inherently embedded in LiDAR point clouds. However, the frequency information is crucial for accurate scatterer generation. Consequently, the frequency information  $f_c$  is processed through a fully connected network and subsequently treated as a patch  $\mathbf{F}_f$ , which is expressed as

$$\mathbf{F}_f = \mathcal{F}(f_c) \in \mathbb{R}^{1 \times D} \quad (12)$$

where  $\mathcal{F}(\cdot)$  represents the fully connected network. Then, the frequency patch is combined with all the other patches, which is expressed as

$$\mathbf{F}_{d,f}^{\text{PE}} = [\mathbf{F}_d^{\text{PE}}, \mathbf{F}_f] \in \mathbb{R}^{(N+1) \times D}. \quad (13)$$

### C. Backbone Network

Pre-trained LLMs are powerful tools capable of tackling various cross-modal downstream tasks by leveraging their vast



knowledge base. Compared to smaller models, LLMs offer superior ability to capture complex patterns, handle subtle cross-modal relationships, and deliver more robust/reliable performance. For example, GPT-2 [30] is built on the transformer architecture, which employs self-attention mechanisms to process and generate text. The model consists of multiple layers of transformer blocks, each containing multi-head self-attention and feedforward neural networks. This architecture allows GPT-2 to adequately capture long-range dependencies and contextual information. The input of GPT-2 is tokenized text, which is embedded into high-dimensional vectors. These embeddings are then processed through stacked transformer layers, where each layer applies self-attention to weigh the importance of different words in the context. The output is generated through a linear layer followed by a softmax function, which can predict the next token in the sequence.

Due to the inherent differences between sensing data and language data, GPT-2 cannot be directly applied to these tasks. To overcome this challenge, similar to the tokenization of text data, the preprocessing and embedding for sensing data through the proposed preprocessor and embedding module are generated. The preprocessed LiDAR point cloud “tokens” are then fed into the backbone of the GPT-2

$$\mathbf{F}^{\text{LLM}} = \mathcal{LLM}(\mathbf{F}_{\text{d,f}}^{\text{PE}}) \quad (14)$$

where  $\mathcal{LLM}(\cdot)$  represents backbone networks, i.e., the first  $N_L$  layers of GPT-2. In the proposed model, GPT-2 layers can be replaced with other LLMs. This is because that LiDAR point clouds are transformed into a unified token format, which allows for flexibility and compatibility. When choosing an alternative model, it is essential to strike a balance between performance and computational overhead.

#### D. Output Module

The output of the network is a single-layer grid map, which represents the spatial distribution of scatterers. The dimension of the grid map is  $n^x \times n^y$  and the length and width of grid  $g_s^{x,y}(t)$  can be calculated as

$$x'_g(t) = \frac{x_{\max}(t) - x_{\min}(t)}{n^x} \quad (15)$$

$$y'_g(t) = \frac{y_{\max}(t) - y_{\min}(t)}{n^y}. \quad (16)$$

Scatterers within the VR are dropped onto the corresponding grid. The density of scatterers in each grid is calculated as

$$\phi_g(t) = \frac{|\mathbb{S}^g(t)|}{x'_g(t) \times y'_g(t)} \quad (17)$$

where  $\mathbb{S}^g(t)$  is the scatterer set corresponding to each grid and  $|\cdot|$  denotes the number of elements in a set. The output module is designed to convert the output features of the LLM into the scatterer grid maps, which can be expressed as

$$\hat{\phi}_g(t) = \mathcal{C}(\mathcal{LR}(\mathcal{C}(\mathcal{V}(\mathbf{F}^{\text{LLM}})))) \in \mathbb{R}^{n^x \times n^y} \quad (18)$$

where  $\mathcal{LR}(\cdot)$  represent a LeakyReLU operation [31]. Note that the reasoning capabilities of LLMs hold promise for achieving higher-resolution generation of scatterer grids.

TABLE I  
HYPER-PARAMETER FOR NETWORK DESIGN

Parameter	Value
Size of LiDAR point cloud feature grid maps@[3, $m^x$ , $m^y$ ]	[3, 80, 80]
Size of scatterer grid maps@[1, $n^x$ , $n^y$ ]	[1, 10, 10]
Size of convolution kernels in embedding module@ $kernel\_size$	(8, 8)
Size of convolution kernels in output module@ $kernel\_size$	(1, 1)
GPT-2 feature dimension@ $D$	768
The number of GPT-2 layers@ $N_L$	6

## IV. EXPERIMENTS

In this section, the simulation settings are illustrated and then the performance of the proposed LLM4SG method is evaluated.

### A. Setup

1) *Dataset Overview*: To organize the V2V-M3 dataset, data entries will be named according to specific scenario conditions, including scenario name, frequency band, and VTD. Each dataset entry will reflect a unique combination of these conditions, which helps to clarify the selection of datasets in the following text. The naming convention follow a structure like ScenarioName\_FrequencyBand\_VTD, e.g., Cross-road\_28GHz\_HighVTD, ForkingRoad\_sub6GHz\_LowVTD. The V2V-M3 dataset for each condition includes 27,000 samples, comprising 18 transceiver pairs over 1500 snapshots. In each sample, three-layer LiDAR point cloud feature grid maps are utilized as network input, while the single-layer scatterer grid map serves as the network output.

2) *Baseline*: The original model embedding module and backbone network are replaced with ResNet to establish a baseline for comparison. This modification utilizes ResNet’s deep residual connections, which facilitate effective feature capture and gradient flow. Using ResNet as the baseline provides a consistent reference point to evaluate performance improvements.

3) *Network and Training Configuration*: Table I presents the hyper-parameters for the LLM4SG network, detailing the dimensions of the LiDAR point cloud feature grid maps, the dimensions of the scatterer grid map, and the architectural specifics of the ScaR network. The smallest version of GPT-2, which has a feature dimension of  $F = 768$ , is employed, with only the first  $N = 6$  layers being used. Table II outlines the hyper-parameters used for fine-tuning the LLM4SG network. The network is trained using PyTorch with the Adaptive Moment Estimation (ADAM) optimizer [32]. The dataset for each condition is split into training, validation, and test sets in a 4:1:1 ratio. The model performance is assessed after training on the training set, and hyperparameters are tuned using the validation set. The test set evaluates the network’s generalization ability on previously unseen data. It’s important

TABLE II  
HYPER-PARAMETER FOR NETWORK FINE-TUNING

Parameter	Value
Batch size	256
Starting learning rate	$1 \times 10^{-2}$
Learning rate scheduler	Per 150 epochs
Learning-rate decaying factor	0.1
Epochs	600
Optimizer	ADAM
Loss function	NMSELoss

to point out that in the pre-trained GPT-2 model, the self-attention and feed-forward layers are kept frozen, while the remaining parameters are trainable. Since these frozen layers contain the majority of the model's parameters, the number of trainable parameters is relatively limited.

4) *Loss Function*: In this model, the output is a  $n^x \times n^y$  scatterer grid map. The loss function is based on the normalized mean squared error (NMSE) of each grid's predicted value compared to the ground truth, which can be calculated as

$$NMSE(\phi_g, \hat{\phi}_g) = \frac{\sum_{i=1}^N (\phi_g - \hat{\phi}_g)^2}{\sum_{i=1}^N \phi_g^2}. \quad (19)$$

The NMSE provides a smooth and continuous gradient, which allows optimization algorithms to converge more efficiently during training.

5) *Performance Metric*: To evaluate the performance of LLM4SG, two aspects of performance need to be considered. First, the evaluation focuses on the accuracy of predicting scatterer locations, namely, whether each cell in the grid map correctly indicates the presence of scatterers. The location evaluation metric can be expressed as

$$P_{\text{pos}} = \frac{N_z + N_{\text{nz}}}{n^x \times n^y} \quad (20)$$

where  $N_z$  represents the number of grids whose predicted values and ground truth are both zero and  $N_{\text{nz}}$  represents the number of grids whose predicted values and ground truth are both non-zero. Second, the accuracy of predicting the number of scatterers within each grid is examined. Specifically, the number evaluation metric is defined as the proportion of grids where the predicted number deviates from the ground truth by less than a specified threshold  $S_{\text{th}}$ . The number evaluation metric is calculated as

$$P_{\text{num}} = \frac{|\{g_s^{x,y}(t) | \frac{|\phi_g(t) - \hat{\phi}_g(t)|}{\phi_g(t)} < S_{\text{th}}\}|}{|\{g_s^{x,y}(t)\}|} \quad (21)$$

where  $|\cdot|$  denotes the number of elements in a set.

### B. Performance of LLM4SG Across Individual Conditions

The performance of LLM4SG is evaluated under individual environmental conditions, including different scenarios, frequency bands, and VTDs. We performed experiments

using various hyper-parameter values and selected the optimal results for comparison. The  $P_{\text{pos}}$  and  $P_{\text{num}}$  results in the crossroad and forking road are shown in Table III and Table IV, respectively. The charts reveal that LLM4SG maintains high performance across different environments, demonstrating strong robustness and adaptability. Meanwhile, experimental results reveal that the performance varies under different environmental conditions. Specifically, the generation accuracy is slightly higher in suburban forking road compared to urban crossroad, due to the low signal interference and multipath effects in suburban. Moreover, the model achieves improved performance under low VTDs, attributed to the less congested environments and diminished interference, which simplify the channel characteristics compared to high VTD scenarios. Furthermore, the model performs better at lower frequencies, as high-frequency signals are more vulnerable to atmospheric absorption and propagation losses, making scatterer generation more difficult.

### C. Performance of LLM4SG in Scenario Condition Transfer

To evaluate the generalization ability of LLM4SG, its performance across different frequency bands, scenarios, and VTD transfers is assessed.

1) *Performance Comparison in Frequency Band Transfer*: The performance of LLM4SG is evaluated in frequency band transfer learning between 28 GHz and sub-6 GHz bands. A few-shot learning approach is used, where the model is initially trained on one frequency band and then fine-tuned with a limited number of samples from the target band. This method assesses the adaptability of the model to distinct frequency bands with minimal additional data. The performance of LLM4SG is compared to that of the baseline across different few-shot sample numbers in crossroad and forking road, as shown in Fig. 6 and Fig. 7. Results indicate that, while both models benefit from few-shot adaptation, LLM4SG consistently outperforms the baseline, especially with minimal few-shot data. These results underscore the superior ability of LLM4SG to generalize effectively across the 28 GHz and sub-6 GHz bands with minimal tuning. These results further demonstrate that adapting from the sub-6 GHz band to 28 GHz enables LLM4SG to exceed the full-sample performance of ResNet with significantly fewer samples, whereas the reverse direction requires more data to achieve the same effect. This asymmetry is due to the lower path loss and richer multipath characteristics of sub-6 GHz channels, which offer more informative and diverse training samples for cross-frequency generalization.

2) *Performance Comparison in Scenario Transfer*: The performance of the LLM4SG model is evaluated in scenario transfer learning between three distinct environments, namely urban crossroad, suburban forking road, and urban wide lane [33]. The model is first trained on one scenario and then fine-tuned with a limited number of samples from another scenario. Unlike the frequency band transfer, where the focus was on channel characteristics, this transfer challenges the model's ability to adapt to entirely different spatial and environmental features. The performance of LLM4SG is compared to that



TABLE III  
PERFORMANCE OF THE LLM4SG UNDER VARIOUS ENVIRONMENTAL CONDITIONS IN CROSSROAD

Model	Crossroad_28GHz_HighVTD		Crossroad_28GHz_LowVTD		Crossroad_sub6GHz_HighVTD		Crossroad_sub6GHz_LowVTD	
	$P_{pos}$	$P_{num}$	$P_{pos}$	$P_{num}$	$P_{pos}$	$P_{num}$	$P_{pos}$	$P_{num}$
ResNet	91.5%	86.2%	92.6%	88.1%	88.5%	80.2%	91.8%	85.2%
LLM4SG	<b>96.9%</b>	<b>94.8%</b>	<b>97.1%</b>	<b>95.7%</b>	<b>93.1%</b>	<b>86.3%</b>	<b>97.4%</b>	<b>94.8%</b>

TABLE IV  
PERFORMANCE OF THE LLM4SG UNDER VARIOUS ENVIRONMENTAL CONDITIONS IN FORKING ROAD

Model	ForkingRoad_28GHz_HighVTD		ForkingRoad_28GHz_LowVTD		ForkingRoad_sub6GHz_HighVTD		ForkingRoad_sub6GHz_LowVTD	
	$P_{pos}$	$P_{num}$	$P_{pos}$	$P_{num}$	$P_{pos}$	$P_{num}$	$P_{pos}$	$P_{num}$
ResNet	88.1%	83.2%	89.9%	85.5%	89.2%	84.7%	89.8%	85.8%
LLM4SG	<b>94.7%</b>	<b>92.8%</b>	<b>95.1%</b>	<b>93.2%</b>	<b>93.7%</b>	<b>91.4%</b>	<b>94.6%</b>	<b>92.1%</b>

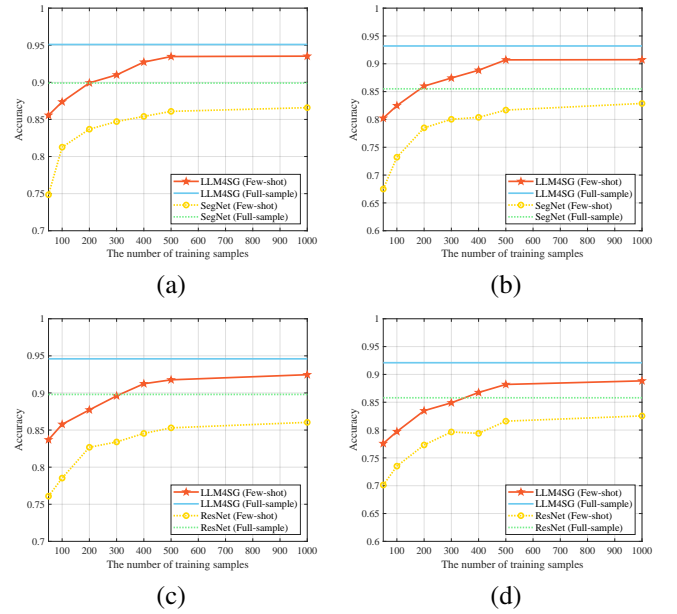
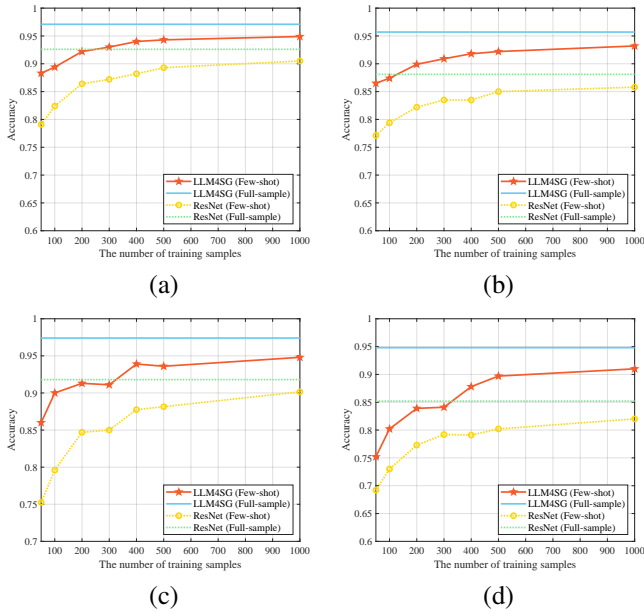


Fig. 6. Generalization performance in frequency band transfer in urban crossroad. (a) Location evaluation metric from sub-6 GHz to 28 GHz. (b) Number evaluation metric from sub-6 GHz to 28 GHz. (c) Location evaluation metric from 28 GHz to sub-6 GHz. (d) Number evaluation metric from 28 GHz to sub-6 GHz.

Fig. 7. Generalization performance in frequency band transfer in suburban forking road. (a) Location evaluation metric from sub-6 GHz to 28 GHz. (b) Number evaluation metric from sub-6 GHz to 28 GHz. (c) Location evaluation metric from 28 GHz to sub-6 GHz. (d) Number evaluation metric from 28 GHz to sub-6 GHz.

of the baseline across different few-shot sample numbers, as shown in Fig. 8 and Fig. 9. Simulation results show that LLM4SG more effectively captures generalizable features across the aforementioned scenarios and demonstrates greater adaptability, especially when data is limited. This highlights the model's ability to generalize across environments with varying road layouts and traffic patterns. The complexity of the scenarios decreases from wide lane to crossroad and then to forking road. In this order, transferring from a more complex to a simpler scenario requires fewer training samples for LLM4SG to outperform ResNet trained with full samples. This is because complex scenarios include more varied objects, occlusions, signal reflections, and dynamic changes, which help the model learn more useful and general features.

3) *Performance Comparison in Vehicular Traffic Density Transfer:* The performance of the LLM4SG is evaluated on VTD transfer between high and low VTD conditions. The

analysis evaluates the adaptability of LLM4SG to changing traffic conditions by training on one VTD and testing on another. The performance of LLM4SG is compared to that of the baseline across different few-shot sample numbers, as shown in Fig. 10. Simulation results show that performance on the target VTD consistently improves with more transfer samples. Notably, LLM4SG achieves better adaptation across VTD conditions than the baseline, particularly with minimal few-shot data. Furthermore, generalization from high VTDs to low VTDs requires fewer training samples compared to the reverse direction. This is because high VTD scenarios are inherently more complex, with richer multipath propagation and greater mobility, allowing the model to learn more comprehensive and transferable features during training.

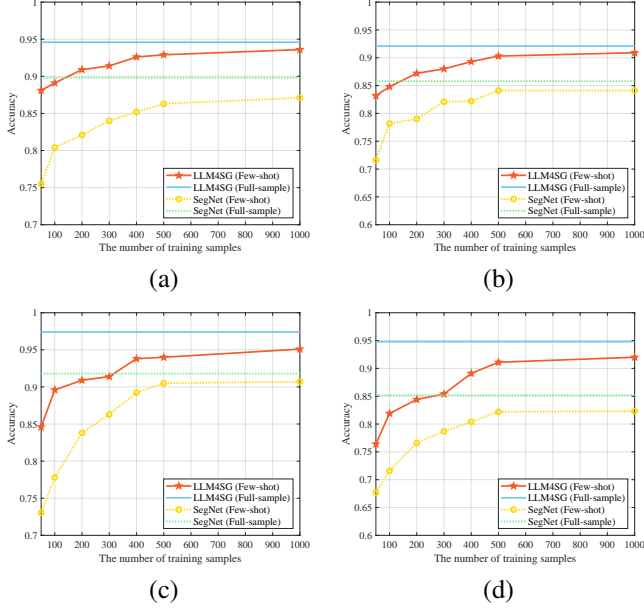


Fig. 8. Generalization performance in scenario transfer. (a) Location evaluation metric from urban crossroad to suburban forking road. (b) Number evaluation metric from urban crossroad to suburban forking road. (c) Location evaluation metric from suburban forking road to urban crossroad. (d) Number evaluation metric from suburban forking road to urban crossroad.

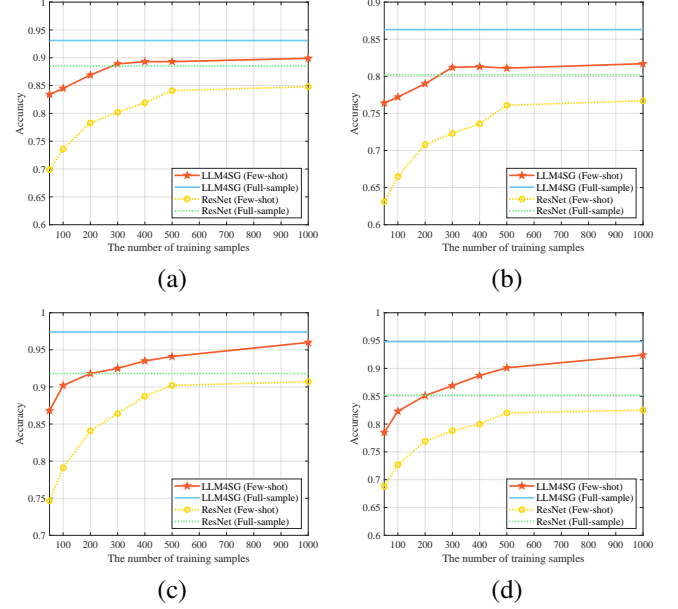


Fig. 10. Generalization performance in VTD transfer in urban crossroad. (a) Location evaluation metric from low VTDs to high VTDs. (b) Number evaluation metric from low VTDs to high VTDs. (c) Location evaluation metric from high VTDs to low VTDs. (d) Number evaluation metric from high VTDs to low VTDs.

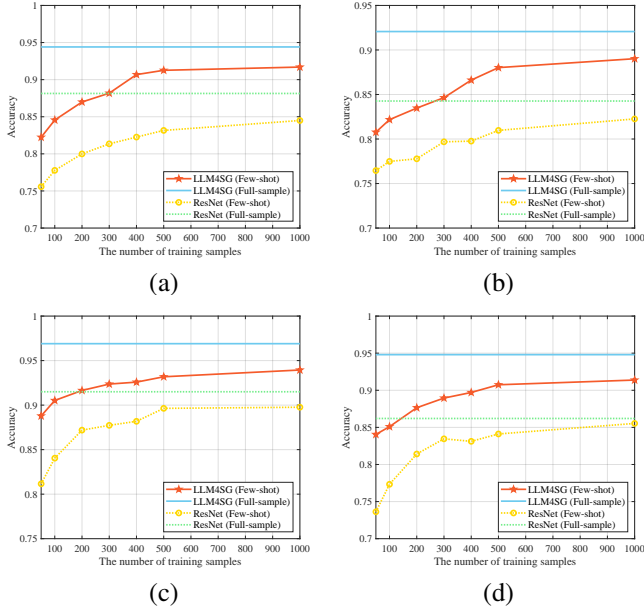


Fig. 9. Generalization performance in scenario transfer. (a) Location evaluation metric from urban crossroad to urban wide lane. (b) Number evaluation metric from urban crossroad to urban wide lane. (c) Location evaluation metric from urban wide lane to urban crossroad. (d) Number evaluation metric from urban wide lane to urban crossroad.

#### D. Ablation Experiments

To assess the effectiveness of specific components, ablation experiments are performed by removing each key module, i.e., patching, positional embedding, and the LLM, as detailed in Table V. The NMSE performance for the test set is recorded. For the LLM4SG without patching, the data was input directly without segmentation. For the LLM4SG without

positional embedding, all position-specific information was excluded from the input data. For the LLM4SG without the LLM module, the pre-trained LLM was removed, with other network components left unchanged. The results show that removing any of these three components led to a decline in performance, underscoring the importance of each for achieving high predictive accuracy.

#### E. Network Storage and Inference Cost

The parameters of models and training and inference time cost by models are closely related to the storage and computational overhead. The number of parameters and training and inference time of LLM4SG and the baseline are shown in Table VI, where training and inference samples are taken from urban crossroad. It can be observed that LLM4SG unfreezes only a small portion of parameters during training, resulting in a lower training overhead compared to the baseline. Meanwhile, LLM4SG has a comparable inference time with the baseline.

#### F. Application Case

1) *Intelligent Channel Modeling*: Conventional channel modeling can be classified into geometry-based deterministic modeling (GBDM), non-geometry stochastic modeling (NGSM), and geometry-based stochastic modeling (GBSM) [18]. The GBDM-based channel model is constructed in a deterministic manner for a specific scenario and leads to high complexity. To reduce the complexity, the NGSM-based channel model determines channel parameters in a stochastic manner and the GBSM-based channel model utilizes the predefined stochastic distribution of scatterers/clusters in the

TABLE V  
RESULTS OF ABLATION EXPERIMENTS

Model	Crossroad_28GHz _HighVTD		Crossroad_28GHz _LowVTD		Crossroad_sub6GHz _HighVTD		Crossroad_sub6GHz _LowVTD	
	$P_{\text{pos}}$	$P_{\text{num}}$	$P_{\text{pos}}$	$P_{\text{num}}$	$P_{\text{pos}}$	$P_{\text{num}}$	$P_{\text{pos}}$	$P_{\text{num}}$
LLM4SG	<b>96.9%</b>	<b>94.8%</b>	<b>97.1%</b>	<b>95.7%</b>	<b>93.1%</b>	<b>86.3%</b>	<b>97.4%</b>	<b>94.8%</b>
w/o patching	91.6%	86.0%	91.8%	87.2%	88.2%	79.8%	92.1%	88.7%
w/o positional embedding	68.5%	63.3%	69.1%	65.4%	62.7%	58.3%	65.4%	68.8%
w/o LLM	83.4%	79.5%	83.8%	81.5%	79.3%	74.9%	82.5%	79.6%

TABLE VI  
NETWORK PARAMETERS AND TRAINING AND INFERENCE TIME PER  
SNAPSHOT

	Parameters (M)	Training time (ms)	Inference time (ms)
LLM4SG	5.08/86.19	19.41	7.96
ResNet	23.53/23.53	22.8	5.67

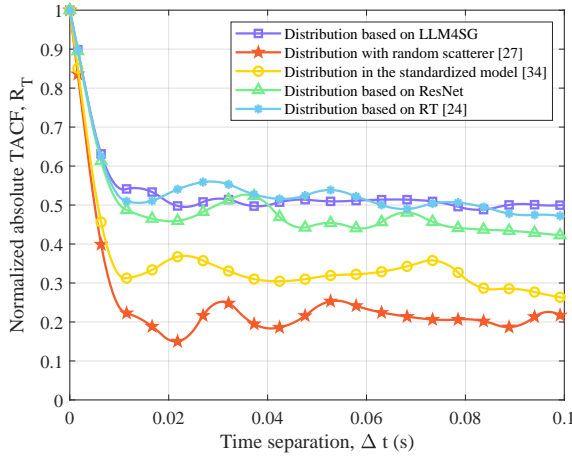


Fig. 11. Comparison of simulated TACFs and RT-based TACFs.

propagation environment. However, the accuracy of stochastic models is limited due to the random generation and determination of channel parameters. LLM4SG provides a novel method to generate scatterers accurately and rapidly. We can exploit the predicted scatterer grid map  $\hat{\phi}_g(t)$  to generate scatterers instead of the predefined stochastic distribution. Based on the channel model proposed in [27] and scatterers generated through different methods, the time auto-correlation function (TACF) generated based on the random statistical distribution of scatterers and TACF based on scatterers from LLM4SG are derived. Then, the RT-based TACF [24] and TACF obtained from standardized models [34] are compared with the aforementioned TACF, as shown in Fig. 11. It can be seen that the TACF based on scatterers from LLM4SG that captures time consistency can achieve a close fit with the RT-based TACF.

2) *Doppler Shift Compensation of High-Mobility Communications in ITSs*: The proposed scatterer generation model is leveraged to perform Doppler shift compensation in urban crossroad. Specifically, by analyzing the variation between LiDAR point clouds from consecutive snapshots, we compute the velocities of surrounding objects near the Tx and Rx. The positions of scatterers are then predicted using LLM4SG

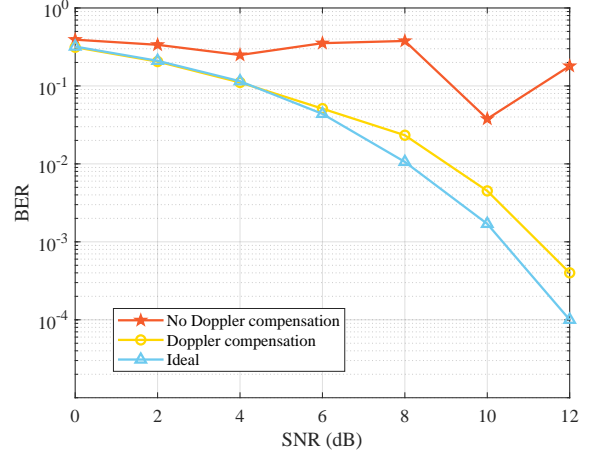


Fig. 12. BER performance of the proposed scheme.

and matched with the LiDAR point clouds to identify the moving objects that significantly impact the communication link. Based on the motion directions and velocities of these effective scatterers, along with those of the Tx and Rx, the Doppler shifts are calculated and compensated. Finally, the improvement in bit error rate (BER) under a QPSK system is evaluated, as shown in Fig. 12. A significant reduction in BER is observed compared to the uncompensated case.

## V. CONCLUSIONS

Based on a new intelligent sensing-communication integration dataset, i.e., V2V-M3, a novel method, named LLM4SG, has been developed to recognize the high-resolution spatial attribute of scatterers from LiDAR point clouds. The network of LLM4SG has been fine-tuned with most of the parameters of the pre-trained LLM kept frozen to achieve intelligent sensing-communication integration utilizing the general knowledge of LLMs. Simulation results have indicated that the proposed LLM4SG has delivered outstanding performance across full-sample and generalization testing. The developed LLM4SG has achieved over 93% accuracy in scatterer position generation and over 85% accuracy in scatterer quantity generation. Moreover, the results have demonstrated the strong few-shot and generalization capabilities of LLM4SG, with the model consistently surpassing small models in knowledge transfer across different VTDs, frequency bands, and ITS scenarios, showing an improvement of over 9%. The advanced architectures of LLMs support deep contextual understanding, allowing them to adapt to varying conditions with minimal

retraining. This flexibility ensures reliable generation in high-mobility real-world V2V scenarios in ITSs. Dedicated modules designed in LLM4SG strategically leverage these strengths to achieve accurate scatterer generation.

## REFERENCES

- [1] F.-Y. Wang *et al.*, “Transportation 5.0: The DAO to safe, secure, and sustainable intelligent transportation systems,” *IEEE Trans. Intell. Transport. Syst.*, vol. 24, no. 10, pp. 10262–10278, Oct. 2023.
- [2] H. Li *et al.*, “Transportation internet: A sustainable solution for intelligent transportation systems,” *IEEE Trans. Intell. Transport. Syst.*, vol. 24, no. 12, pp. 15818–15829, Dec. 2023.
- [3] X. Cheng, Z. Huang, and L. Bai, “Channel nonstationarity and consistency for beyond 5G and 6G: A survey,” *IEEE Commun. Surveys Tuts.*, vol. 24, no. 3, pp. 1634–1669, Thirdquarter 2022.
- [4] M. Yang *et al.*, “A cluster-based three-dimensional channel model for vehicle-to-vehicle communications,” *IEEE Trans. Veh. Technol.*, vol. 68, no. 6, pp. 5208–5220, Jun. 2019.
- [5] Z. Huang and X. Cheng, “A general 3D space-time-frequency non-stationary model for 6G channels,” *IEEE Trans. Wireless Commun.*, vol. 20, no. 1, pp. 535–548, Jan. 2021.
- [6] Y.-X. Wang, Z.-Y. Liu, and L.-X. Guo, “Research on MIMO channel capacity in complex indoor environment based on deterministic channel model,” in *Proc. IEEE/CIC International Conference on Communications in China (ICCC’21 Workshops)*, Xiamen, China, 2021, pp. 405–409.
- [7] Q. Zhang, T. H. Loh, Z. Huang, and F. Qin, “An investigation into the spatial heterogeneity of MIMO device with 3D deterministic channel modelling using single-probe anechoic chamber method,” in *Proc. European Conference on Antennas and Propagation (EuCAP’23)*, Florence, Italy, Mar. 2023, pp. 1–5.
- [8] L. Jiao *et al.*, “Advanced deep learning models for 6G: Overview, opportunities, and challenges,” *IEEE Access*, vol. 12, pp. 133245–133314, Jun. 2024.
- [9] G. Sun *et al.*, “Dynamic clustering of multipath components for time-varying propagation channels,” *IEEE Trans. Veh. Technol.*, vol. 70, no. 12, pp. 13396–13400, Dec. 2021.
- [10] M. Yang *et al.*, “Machine-learning-based fast angle-of-arrival recognition for vehicular communications,” *IEEE Trans. Veh. Technol.*, vol. 70, no. 2, pp. 1592–1605, Feb. 2021.
- [11] M. González-Palacio *et al.*, “Machine-learning-based combined path loss and shadowing model in LoRaWAN for energy efficiency enhancement,” *IEEE Internet Things J.*, vol. 10, no. 12, pp. 10725–10739, Jun. 2023.
- [12] Y. Lee *et al.*, “Deep learning based modeling of wireless communication channel with fading,” in *Proc. International Wireless Communications and Mobile Computing (IWCMC’24)*, Ayia Napa, Cyprus, May 2024, pp. 1577–1582.
- [13] Y. Zhang *et al.*, “Generative adversarial networks based digital twin channel modeling for intelligent communication networks,” *China Commun.*, vol. 20, no. 8, pp. 32–43, Aug. 2023.
- [14] P. Kumari, J. Choi, N. González-Prelcic, and R. W. Heath, “IEEE 802.11ad-based radar: An approach to joint vehicular communication-radar system,” *IEEE Trans. Veh. Technol.*, vol. 67, no. 4, pp. 3012–3027, Apr. 2018.
- [15] B. Li and A. P. Petropulu, “Joint transmit designs for coexistence of MIMO wireless communications and sparse sensing radars in clutter,” *IEEE Trans. Aerosp. Electron. Syst.*, vol. 53, no. 6, pp. 2846–2864, Dec. 2017.
- [16] N. Nartasilpa, A. Salim, D. Tuninetti, and N. Devroye, “Communications system performance and design in the presence of radar interference,” *IEEE Trans. Commun.*, vol. 66, no. 9, pp. 4170–4185, Sept. 2018.
- [17] X. Cheng *et al.*, “Intelligent multi-modal sensing-communication integration: Synesthesia of Machines,” *IEEE Commun. Surveys Tuts.*, vol. 26, no. 1, pp. 258–301, Firstquarter 2024.
- [18] L. Bai *et al.*, “Multi-modal intelligent channel modeling: A new modeling paradigm via Synesthesia of Machines,” *IEEE Commun. Surveys Tuts.*, accepted, 2025.
- [19] Z. Huang, L. Bai, Z. Han, and X. Cheng, “Scatterer recognition for multi-modal intelligent vehicular channel modeling via Synesthesia of Machines,” *IEEE Wirel. Commun. Lett.*, accepted, 2025.
- [20] K. Lu, A. Grover, P. Abbeel, and I. Mordatch, “Pretrained transformers as universal computation engines,” *arXiv preprint arXiv:2103.05247*, vol. 1, 2021.
- [21] T. Brown *et al.*, “Language models are few-shot learners,” *Adv. Neural Inf. Process. Syst.*, vol. 33, pp. 1877–1901, 2020.
- [22] B. Liu *et al.*, “LLM4CP: Adapting large language models for channel prediction,” *J. Commun. Inf. Netw.*, vol. 9, no. 2, pp. 113–125, Jun. 2024.
- [23] S. Fan *et al.*, “Csi-LLM: A novel downlink channel prediction method aligned with LLM pre-training,” *arXiv preprint arXiv:2409.00005*, 2024.
- [24] Remcom. Wireless InSite. [Online]. Available: <https://www.remcom.com/wireless-insite-em-propagation-software> [Publication date: Jan. 2017, Accessed date: Mar. 2022].
- [25] S. Shah, D. Dey, C. Lovett, and A. Kapoor, “AirSim: High-fidelity visual and physical simulation for autonomous vehicles,” in *Field and Service Robotics*, M. Hutter and R. Siegwart, Eds. Cham, Switzerland: Springer, 2018, pp. 621–635.
- [26] X. Cheng *et al.*, “M<sup>3</sup>SC: A generic dataset for mixed multi-modal (MMM) sensing and communication integration,” *China Commun.*, vol. 20, no. 11, pp. 13–29, Nov. 2023.
- [27] L. Bai, M. Lu, Z. Huang, and X. Cheng, “A multi-modal UAV-to-ground channel model for 6G intelligent sensing-communication integration,” *IEEE Trans. Commun.*, submitted for publication, 2025.
- [28] H. Jiang *et al.*, “In defense of grid features for visual question answering,” in *Proc. IEEE Conference on Computer Vision and Pattern Recognition (CVPR’20)*, Seattle, WA, USA, Jun. 2020, pp. 10267–10276.
- [29] A. Vaswani *et al.*, “Attention is all you need,” *Adv. Neural Inf. Process. Syst.*, vol. 30, pp. 5998–6008, 2017.
- [30] A. Radford *et al.*, “Language models are unsupervised multitask learners,” *OpenAI blog*, vol. 1, no. 8, pp. 1–9, 2019.
- [31] J. Xu *et al.*, “Reluplex made more practical: Leaky ReLU,” in *Proc. IEEE Symposium on Computers and Communications (ISCC’20)*, Rennes, France, Jul. 2020, pp. 1–7.
- [32] D. P. Kingma and J. Ba, “Adam: A method for stochastic optimization,” in *Proc. Int. Conf. Learn. Represent.*, May. 2015, pp. 1–12.
- [33] X. Cheng *et al.*, “SynthSoM: A synthetic intelligent multi-modal sensing-communication dataset for Synesthesia of Machines (SoM),” *Sci. Data*, accepted, 2025.
- [34] Technical Specification Group Radio Access Network; Study on Channel Model for Frequencies From 0.5 to 100 GHz (Release 14), document TR 38.901 Version 14.2.0, 3GPP, Sep. 2017. [Online]. Available: <http://www.3gpp.org/DynaReport/38901.htm>.